Journal of Materials Chemistry A

ROYAL SOCIETY OF CHEMISTRY

COMMUNICATION

View Article Online
View Journal | View Issue

Cite this: J. Mater. Chem. A, 2026, 14, 348

Received 1st October 2025
Accepted 19th November 2025

DOI: 10.1039/d5ta08057f

rsc.li/materials-a

Consecutive intra-particle phase transitions in the $LiFePO_4$ battery electrode material

Souzan Hammadi, [a] Nana Ofori-Opoku, [b] Daniel Brandell [a] and Peter Broqvist *[a]

Mesoscale modeling of battery electrode materials requires accurate free energy data. Typical models employed assume the regular solution model, which accounts for ideal mixing entropy and weak interactions from the enthalpic contribution. However, this free energy description is insufficient when describing the $LiFePO_4$ electrode due to the electrostatic interactions between its ionic species. This study addresses the asymmetry in the experimental phase diagram of $LiFePO_4$, particularly the eutectoid point at 60% Li concentration, which the symmetric regular solution model fails to capture. We employ spline interpolations to capture this more complex free energy landscape within a phase-field model. Our findings reveal that when this asymmetry is accounted for, delithiation occurs through a solid solution pathway, driven by thermodynamic forces that induce an intermediate solid solution phase, thereby challenging the prevailing notion that this phase is only accessible at high charging rates at the nano-scale. The solid solution phase mitigates strain evolution and enhances delithiation rates compared to the conventional model, offering new insights into the phase transformation characteristics of $LiFePO_4$ electrodes.

The $LiFePO_4$ (LFP) intercalation electrode material is expected to dominate parts of the global Li ion battery market in the coming years due to its composition of more abundant elements, lower production costs and more stable electrochemical performance compared to many competing electrode formulations.[1–4] Despite this, many questions persist concerning its physical characteristics at the meso-scale during battery operation. In fact, incorporation of Li into electrode materials is a dynamic process that occurs across multiple scales. Short-range interactions between charged species can trigger phase separation, with the resulting volume changes generating long range strain fields that bridge atomic scale processes with meso-scale effects. This phenomenon is especially evident in LFP electrodes, where coherency strain between the Li-poor $FePO_4$ (FP) phase and the Li-rich $LiFePO_4$ (LFP) phase produces a growing interface during battery operation.[5] The spatial and temporal evolution of the LFP/FP interface can be modeled using the phase-field technique, which derives gradients of concentration and chemical potential from an energy functional.[6–11] This functional incorporates the thermodynamic free energy description that dictates the outcome of the intercalation process even under conditions far from equilibrium.

Traditionally, the free energy is modeled using the regular solution approach, which assumes an ideal mixing entropy and an enthalpic contribution that is characteristic of weak interactions between species.[12] However, since battery electrode materials comprise charged ions, their electrostatic interactions can lead to various degrees of short-range order as a function of Li concentration.[13–16] Consequently, a more complex free energy landscape is expected.[17] This complexity is evident in the LFP system, where a multitude of different free energy descriptions have been proposed in the literature.[17–21].

Despite its simplified free energy description, all phase-field models of LFP electrodes in the literature employ the regular solution model.[6–11] The choice is driven by three conventional phase-field modeling requirements: (1) the energy must be differentiable and hence continuous, (2) it must remain bounded at the limits, and (3) its derivatives must also be continuous. A key advantage of the regular solution model is its ease of implementation; it requires only one parameter, Ω (see the SI), that naturally constrains the Li fraction to the interval [0,1] *via* the natural logarithm terms, ensuring smooth behavior and continuous derivatives. Additionally, its widespread use is reinforced by the limited availability of open-source free energy data in the literature. While there are indeed multiple studies presenting alternative formulations of the free energy, the necessary data are often not readily accessible: parameters may be missing,[18] a minimization procedure might be required,[20] or a dedicated database must be constructed.[19]

To overcome these challenges, we directly extract data points from published studies and use spline interpolations to

[a]Department of Chemistry –Ångström Laboratory, Uppsala University, 75121 Uppsala, Sweden. E-mail: peter.broqvist@kemi.uu.se

[b]Department of Materials Science and Engineering, Brockhouse Institute for Materials Research, McMaster University, Hamilton, L8S 1L4, Canada

generate continuous piecewise functional forms of each free energy description. These functions are then integrated into the phase-field model presented in our previous work to evaluate their impact on the phase evolution in LFP during delithiation.[6] The Li extraction is dictated by charge transfer at the boundary between the electrode and an artificial electrolyte and is described using the Marcus–Hush–Chidsey model, which results in delithiation at constant applied potentials at varying rates.[22] This approach enables us to discern how various free energy contributions affect both the free energy landscape and the microstructural evolution of the LFP/FP phases within the bulk material. The phase-field model and its parameters are detailed in the SI. In this study, we compare three free energy descriptions at room temperature: the regular solution model,[6,8] the CALPHAD (CALculation of PHAse Diagrams) description by Phan *et al.*,[19] and the free energy description optimized using a machine learning (ML) procedure by Lund *et al.*[20] The resulting spline functions are plotted together in Fig. 1a–c, both with and without isotropic elastic energy. The first derivatives are shown in Fig. 1b–d.

In Fig. 1, the regular solution model shows a symmetric energy profile with two minima at low (FP phase) and high (LFP phase) Li concentration. In contrast, the other two free energy formulations exhibit an additional local minimum at approximately 60% Li concentration. This third minimum corresponds to an additional solid phase, as evidenced by experimental phase diagrams of Delacourt *et al.*[23] and Dodd *et al.*,[24] which clearly identify a eutectoid point at 420–470 K and 60% Li concentration.

The free energy curve obtained from the CALPHAD database by Phan *et al.*[19] presented in Fig. 1a has been parameterized using experimental data. Notably, the phase diagram generated from this database closely aligns with the experimental phase diagram by Dodd *et al.*[24] The ML approach is parameterized on data from the same experimental phase diagram, and despite differences in barrier height to the CALPHAD free energy, both consistently predict the highest energy at approximately 40% Li content and feature a third local minimum at 60%.

The CALPHAD energy landscape of LFP across composition and temperature is modeled as a solution phase.[19] Both end member phases, FP and LFP, have certain solubility of Li and Li vacancies defined by the inflection points of the energy landscape. Likewise, the solid phase near 60% Li exists within a finite concentration range. While the ordered FP and LFP phases display distinct X-ray diffraction patterns, the solid phase at 60% Li concentration, however, shows no evidence of Li ordering in neutron diffraction, X-ray synchrotron, or electron diffraction analyses.[25] This confirms the absence of long-range order and this phase will therefore be referred to as a solid solution throughout this study. Short-range interactions, described as a tendency for Li to cluster near Fe(II) sites, likely stabilize the phase and explain its pronounced metastability at room temperature.[16] In fact, solid solutions are rarely fully disordered; they can be stabilized as the degree of order increases.[26]

Accurately describing phase equilibria is essential, as the free energy fundamentally governs the phase evolution characteristics. In principle, the free energy defines the phase diagram, with common tangents between free energy minima indicating thermodynamic equilibrium between the corresponding phases. While similar energy minima across different free energy descriptions can lead to comparable phase diagrams, variations in barrier heights and the overall curvature of the energy landscape can cause differences in the spatial evolution of phases. This distinction is particularly notable when comparing the regular solution model with the experimentally informed free energy descriptions.

An important contribution to the energy landscape of a solid experiencing coherency strain is the elastic strain energy. Although the strain in the LFP system is highly anisotropic, its impact can be illustrated by assuming an isotropic energy. As illustrated in Fig. 1a–c, this has a significant effect on the energy landscape. In the CALPHAD description (Fig. 1c), the elastic energy shifts the local minima at 60% Li to a global minimum. This effect is further evidenced by the stepwise transition observed in the first derivative of the CALPHAD energy (Fig. 1d). In contrast, the ML-based energy retains its energy barriers even when the elastic energy is considered. It is important to note that these illustrations and observations assume an isotropic approximation from linear elasticity (see the SI), while the actual coherency strain in the LFP system is anisotropic, leading to spatial variations in phase stability—a factor that is accounted for in the phase-field model.

Phase-field simulations of the delithiation process in LFP are presented in Fig. 2, showing a decrease in average Li concentration, voltage and current at three distinct charge transfer rates and free energy descriptions. The discontinuities in the voltage profile, Fig. 2b–e, are attributed to a first-order phase transition that is characterized by nucleation and subsequent growth.[6] In contrast, a second-order transition – indicative of spinodal decomposition – occurs when concentration fluctuations lead to phase separation without nucleation.[27] Both the

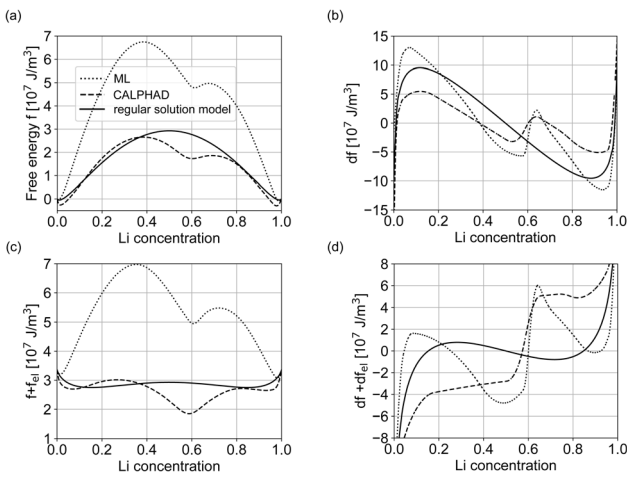

Fig. 1 Spline functions with their respective derivatives, with and without isotropic elastic energy ($f_{elast}^{isotropic}$). (a) The free energy of the regular solution model,[8] the CALPHAD description[19] and the ML model.[20] (b) The first derivative df, (c) the free energy with the elastic energy contribution $f + f_{elast}^{isotropic}$ and (d) the derivative of both contributions df + d$f_{elast}^{isotropic}$.

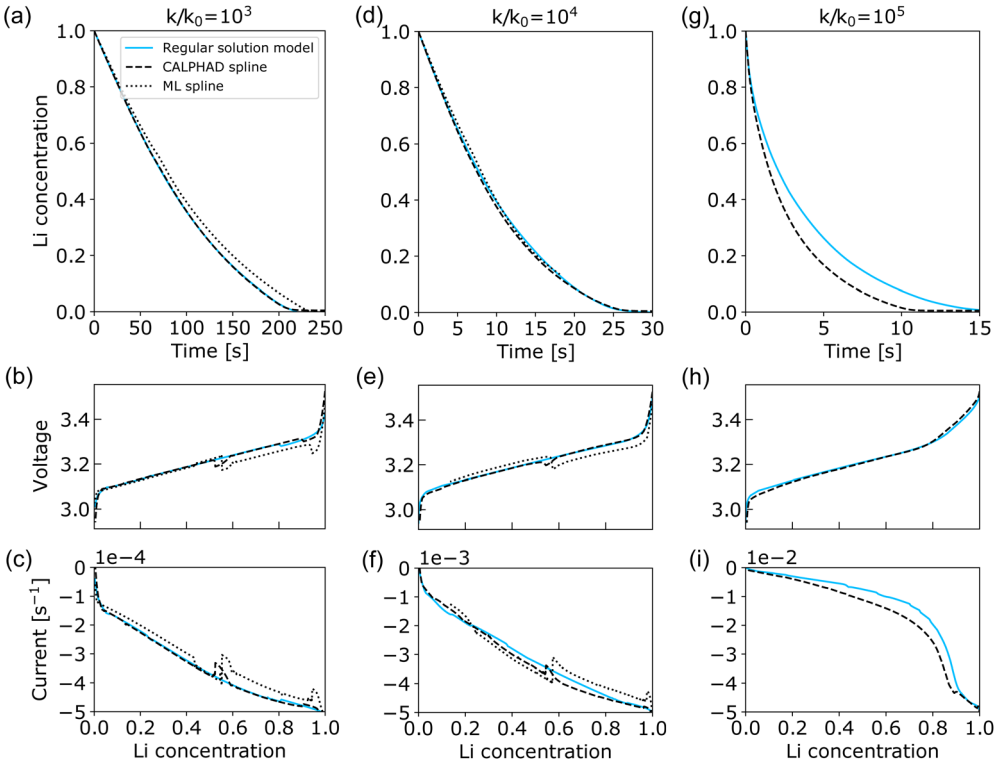

Fig. 2 Phase-field simulations (128 × 64 nm) with coherency strain at different charge transfer rates, (a–c) $k/k_0 = 10^3$, (d–f) $k/k_0 = 10^3$ and (g–i) $k/k_0 = 10^5$. The presented plots show the change in average Li concentration over time, the voltage profile and the current I/FN_A, where F is Faraday's constant and N_A is Avogadro's constant.

voltage profile and current, Fig. 2b–f, exhibit a discontinuity at approximately 60% Li concentration indicating a phase transition happening nearly half-way during the delithiation process. This discontinuity vanishes at $k/k_0 = 10^5$ (Fig. 2h), signaling a transition from a first-order to a second-order phase change. At this rate constant, the CALPHAD-based simulation delithiates faster than the one using the regular solution model, as seen in Fig. 2g. For the regular solution model, this rate represents the onset of mass transport limitation for this particular system, as we previously reported.[6] Overall, at intermediate charge transfer rates, the temporal evolution of the delithiation process is similar across all three energy descriptions. However, the CALPHAD energy permits faster delithiation at higher rates. The reason for this can be further elucidated by observing the microstructural snapshots of the simulations in Fig. 2d–f at $k/k_0 = 10^4$, presented in Fig. 3.

The microstructures presented in Fig. 3 illustrate the spatial evolution of three distinct phases: LFP, FP, and additionally a third intermediate solid solution phase, SS. In simulations employing the regular solution model (Fig. 3a), only two phases are evident, whereas the CALPHAD (Fig. 3b) and ML (Fig. 3c) descriptions display all three, where the third SS phase corresponds to the metastable minima at roughly 60% Li, as shown in the energy landscape in Fig. 1a. Interestingly, even with the ML free energy description, which features a local minimum for the SS regardless of the isotropic elastic energy contribution (Fig. 1c), the SS phase still develops.

This suggests that the transition through this pathway is still highly beneficial for the system. When the delithiation occurs through a solid solution pathway, it first starts by introducing the SS phase. The FP phase starts evolving when the SS phase has completely filled the simulation box, resulting in the evolution of two types of interfaces: one between SS/LFP and

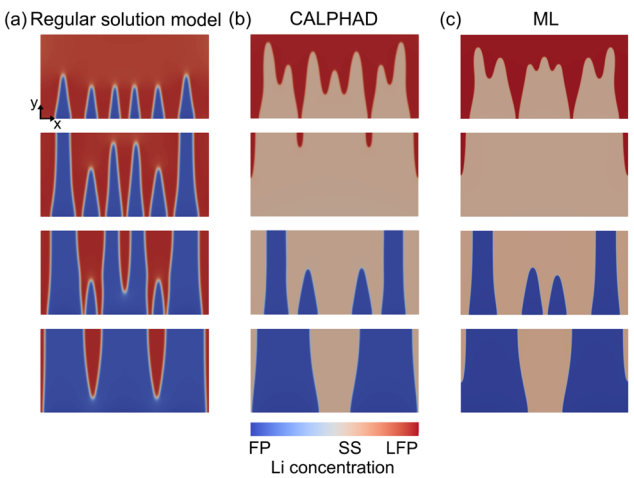

Fig. 3 Snapshots of the microstructure from the phase-field simulations (128 × 64 nm) at $k/k_0 = 10^4$ presented in Fig. 2d using (a) the regular solution model, (b) CALPHAD and (c) ML free energy at 80, 60, 40 and 20% average Li concentration. The delithiation process starts with fully LFP (red) and ends with fully FP (blue). SS stands for solid solution.

one between SS/FP. Overall, the number of transition points of the FP phase differs, depending on the type of free energy description. Fewer transition points of the FP phase are introduced into the system when there is an intermediate SS phase, compared to the case when no such phase exists.

These differing interfaces are critical, as they can markedly influence the mechanical properties of the electrode. This effect is further investigated in simulations at $k/k_0 = 10^5$ (Fig. 2g–i), where snapshots of both the Li concentration and the strain fields are shown in Fig. 4. Additional simulations at lower charge transfer rates using the CALPHAD free energy description are presented in the SI, also showcasing the evolution of the SS phase. At charge transfer rates $k/k_0 = 10^4$ and lower, we observe sequential phase transitions (Fig. 3), first from LFP to SS, and subsequently from SS to FP. The SS/FP interface emerged only once the LFP/SS interface had disappeared. In contrast, at a higher rate of $k/k_0 = 10^5$, Fig. 3b demonstrates that the FP phase evolves concurrently with the presence of both the SS and LFP phases, with the SS phase acting as an intermediate phase evolving in between. The delithiation, thus, proceeds with the collective movement of all three phases. This dynamic evolution under faster kinetics aligns with our previous findings, which showed that higher charge transfer rates promote the formation of more interfaces.[6]

This phenomenon has significant implications for the strain fields shown in Fig. 4. When an intermediate SS phase is present, the overall strain magnitudes are reduced, as seen in Fig. 4b. The highest coherency strain naturally occurs between the Li-rich LFP and Li-poor FP phases due to the inherent lattice mismatch between their crystal structures, which creates spatially varying elastic eigenstrains. Since the SS phase, at roughly 60% Li, is more coherent with both the FP and LFP phases, its presence helps minimize the strain within the system. Reducing this strain is critical for enhancing the mechanical stability during cycling of LFP electrodes.

In fact, the presence of the SS phase has been used to explain the excellent cycling capabilities of nanosized LFP particles. As the volume-to-surface ratio changes with particle size, smaller particles exhibit larger Li solubility.[28–30] At high (dis)charge rates, phase separation may be completely suppressed in nanosized LFP particles (≈190 nm).[31] The suppression was previously demonstrated in a phase-field model by Bai *et al.*[9] using a depth-averaging approximation,[32] where Li insertion occurs preferentially through interfaces, enabling the bulk concentration to converge with that at the surface. In these models, the regular solution model is used to describe the thermodynamic driving force, leading to the interpretation that phase suppression is a size effect stemming from a different mode of Li transport. This approach has thereafter become the standard when modeling the evolution of the SS phase during (dis)charge of the LFP electrode. It is, therefore, generally believed that as particle size increases, bulk transport limitations become more significant, making the formation of a solid solution phase less favorable.

This is further highlighted by electron microscopy studies that have shown a sharp FP/LFP interface in micrometer sized particles.[33,34] In contrast, *in situ* transmission electron microscopy (TEM) studies on LFP nanowires with a diameter of 200–400 nm show the spatial evolution of the solid solution phase from the electrode surface, measuring 20–25 × 20–40 nm in size, and the existence of all three phases within the bulk material.[35] A more recent study using soft X-ray tomography presents three phases in particles 300 nm wide.[36] Particularly, Fig. 4 from the latter study shows the chemical phase

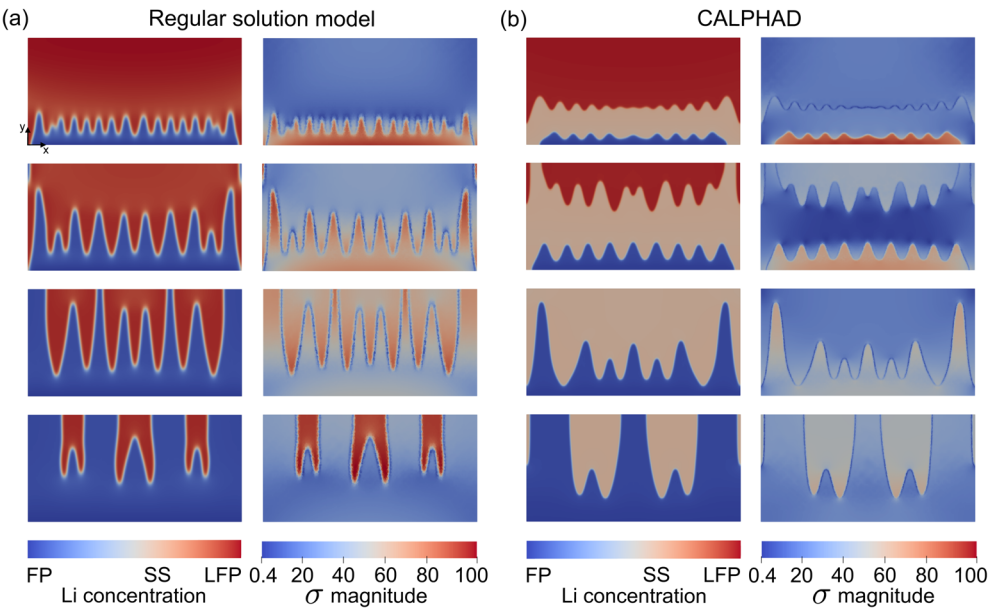

Fig. 4 Microstructure snapshots of the phase-field simulations presented in Fig. 2g (128 × 64 nm) at a higher charge transfer rate $k/k_0 = 10^5$ using (a) the regular solution model and (b) the CALPHAD free energy at 80, 60, 40 and 20% average Li concentration also showing the scaled stress magnitude σ/H, where the maximum value 100 equals 0.72 GPa.

distribution of an individual particle that has striking similarities to the modeled microstructures presented in Fig. 4b, where a mixed phase at a 30–70% Li concentration lies in between regions with either FP or LFP. This intermediate phase was also demonstrated in ref. 37 on particles of size 2000 × 760 nm despite the fact that the particles had been left at room temperature for several months in advance.

We demonstrate that the existence of this phase is purely driven by thermodynamics and we reveal its spatial and temporal evolution during delithiation. The presence of the solid solution phase can, therefore, be expected even in large particles limited by bulk mass transport. However, it has not yet been experimentally observed in systems larger than 2 micrometers, which can be attributed to two effects. Firstly, it may be a finite size effect; the interfacial contribution to the total volume becomes smaller as the particle size increases, reducing the impact of strain mitigation and thereby the advantage of an intermediate solid solution phase. Secondly, larger electrode particles can possess a higher defect density within the bulk,[38] which promotes phase separation.[39] While both effects play a role, we can already confirm the validity of the first. Simulations at larger system sizes, up to six times larger, are presented in Fig. 5. Phase-field results of larger system sizes indeed show that the system can accommodate more interfaces and consequently more strain proving the aforementioned finite size effect.

In the simulated system shown in Fig. 3b at $k/k_0 = 10^4$, the phase transition progresses sequentially from LFP to SS and then to FP, where the FP phase occurs only after the SS fills the entire simulation box. However, when the simulation box is increased sixfold in size (see Fig. 5c), the system behaves differently, with all three phases—LFP, SS, and FP—evolving simultaneously already at 80% average Li concentration. This leads to the compelling question: at what specific particle sizes does the system transition from having an intermediate solid solution phase to a distinct FP/LFP interface?

In this paper, we have evaluated the effect of different free energy descriptions and showed how an additional solid solution phase is introduced when the description contains a third local minima. Simulations without coherency strain in the SI still showcase the intermediate SS phase, which is indicative of it being highly metastable. This shows that three phase coexistence can be achieved purely by the thermodynamic driving force. However, it is not only the thermodynamic driving force that changes with the energy landscape; the mobility also depends on the energy description.[40,41] As for now, it has been assumed to take the form of $M = (DV_m/RT)c(1-c)$. The mobility thus depends on the diffusion coefficient and the $c(1-c)$ term is inherited from the regular solution model. To be rigorous, a changing energy landscape would actually require a change in mobility description. In general, however, this is usually disregarded with the argument that the change in driving force will dominate.

The mobility can also vary in directionality as Li ions favor certain pathways more than others. In this work, we assume 3% anti-site defect density, representing a system where Li and Fe ions change lattice sites, disturbing the otherwise 1D channels Li prefers to travel through.[42] This provides an isotropic mobility.[8,43] This is explored in the SI where simulations are also conducted with a directional Li mobility, showing a more planar phase boundary evolution where the solid-solution phase continues to emerge. Incorporating additional complexity—such as anisotropic gradient energies and careful choice of the mobility description—will be required to achieve quantitative predictions of phase evolution in the LFP system.

To conclude, the free energy description is critical when modeling phase transition behavior in materials. For battery electrode materials, it becomes even more important due to the complex interaction between charged species, which eradicates the use of simple theories like the regular solution model. When more complex free energy descriptions are used, which are based on experimental findings, we see the consecutive evolution of phases, LFP to SS to FP. At a high enough charge transfer rate, all three phases evolve concurrently where the SS phase is an intermediate between FP and LFP. The change in the energy landscape changes the driving force for phase evolution and the three-phase mixture mitigates the otherwise high strain that would exist at the LFP/FP interface. This pushes the point of mass transport limitation and the phase-field model that utilizes the CALPHAD description evolves faster in time.

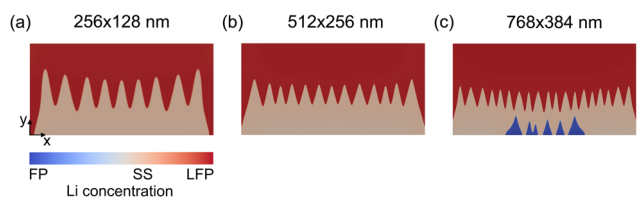

Fig. 5 Microstructure snapshots at 80% average Li concentration showing the increase in interfaces with system size: (a) 256 × 128 nm, (b) 512 × 256 nm and (c) 768 × 384 nm. The phase-field simulations utilize the CALPHAD free energy description and charge transfer is at a rate of $k/k_0 = 10^4$, corresponding to the simulation shown in Fig. 3b.

Conflicts of interest

There are no conflicts to declare.

Data availability

The code and data analysis scripts are available and can be found at GitHub [https://github.com/souzanha/LiFePO4-phase-field].

Supplementary information: detailed descriptions of the phase-field model, theory, implementation and input parameters. The spline interpolations for each model are presented and the computational framework is validated using the regular solution model. See DOI: https://doi.org/10.1039/d5ta08057f.

Acknowledgements

The project was funded by the Swedish Electromobility Center, the National Strategic e-Science program eSSENCE and STandUP for Energy. The Governmental Initiative for Excellence

and Education for the Electrification of the Transport Sector using Battery Technologies (COMPEL) is acknowledged for funding. Computations were performed on resources provided by the National Academic Infrastructure for Supercomputing in Sweden (NAISS) at the National Supercomputer Center (NSC).

Notes and references

1 Z. Li, D. Liu, J. Xiong, L. He, Z. Zhao and D. Wang, *Waste Manage.*, 2020, **107**, 1–8.
2 N. Nitta, F. Wu, J. T. Lee and G. Yushin, *Mater. Today*, 2015, **18**, 252–264.
3 S. Evro, A. Ajumobi, D. Mayon and O. S. Tomomewo, *Future Batteries*, 2024, **4**, 100007.
4 L.-X. Yuan, Z.-H. Wang, W.-X. Zhang, X.-L. Hu, J.-T. Chen, Y.-H. Huang and J. B. Goodenough, *Energy Environ. Sci.*, 2011, **4**, 269–284.
5 A. K. Padhi, K. S. Nanjundaswamy and J. B. Goodenough, *J. Electrochem. Soc.*, 1997, **144**, 1188–1194.
6 S. Hammadi, P. Broqvist, D. Brandell and N. Ofori-Opoku, *J. Mater. Chem. A*, 2025, **13**, 2849–2858.
7 M. Tang, J. F. Belak and M. R. Dorr, *J. Phys. Chem. C*, 2011, **115**, 4922–4926.
8 K. Yang and M. Tang, *J. Mater. Chem. A*, 2020, **8**, 3060–3070.
9 P. Bai, D. A. Cogswell and M. Z. Bazant, *Nano Lett.*, 2011, **11**, 22.
10 S. Daubner, M. Weichel, D. Schneider and B. Nestler, *Electrochim. Acta*, 2022, **421**, 140516.
11 M. J. Welland, D. Karpeyev, D. T. O'Connor and O. Heinonen, *ACS Nano*, 2015, **9**, 9757–9771.
12 H. Lukas, S. G. Fries and B. Sundman, *Computational Thermodynamics: The Calphad Method*, Cambridge University Press, USA, 1st edn, 2007.
13 S. Hammadi, J. Kullgren, M. J. Wolf, D. Brandell and P. Broqvist, *Phys. Rev. B*, 2024, **109**, 144103.
14 F. Zhou, T. Maxisch and G. Ceder, *Phys. Rev. Lett.*, 2006, **97**, 155704.
15 R. Malik, A. Abdellahi and G. Ceder, *J. Electrochem. Soc.*, 2013, **160**, A3179–A3197.
16 J. Cabana, J. Shirakawa, G. Chen, T. J. Richardson and C. P. Grey, *Chem. Mater.*, 2010, **22**, 1249–1262.
17 R. Malik, F. Zhou and G. Ceder, *Nat. Mater.*, 2011, **10**, 587–590.
18 A. Van der Ven, K. Garikipati, S. Kim and M. Wagemaker, *J. Electrochem. Soc.*, 2009, **156**, A949.
19 A. T. Phan, A. E. Gheribi and P. Chartrand, *Can. J. Chem. Eng.*, 2019, **97**, 2224–2233.
20 J. Lund, H. Wang, R. D. Braatz and R. E. García, *Mater. Adv.*, 2022, **3**, 8485–8497.
21 H. Zhao, H. D. Deng, A. E. Cohen, J. Lim, Y. Li, D. Fraggedakis, B. Jiang, B. D. Storey, W. C. Chueh, R. D. Braatz and M. Z. Bazant, Learning heterogeneous reaction kinetics from X-ray videos pixel by pixel., *Nature*, 2023, **621**(7978), 289–294.
22 Y. Zeng, R. B. Smith, P. Bai and M. Z. Bazant, *J. Electroanal. Chem.*, 2014, **735**, 77–83.
23 C. Delacourt, P. Poizot, J.-M. Tarascon and C. Masquelier, *Nat. Mater.*, 2005, **4**, 254–260.
24 J. L. Dodd, R. Yazami and B. Fultz, *Electrochem. Solid-State Lett.*, 2006, **9**, A151.
25 C. Delacourt, J. Rodríguez-Carvajal, B. Schmitt, J.-M. Tarascon and C. Masquelier, *Solid State Sci.*, 2005, **7**, 1506–1516.
26 M. Hillert, *Phase Equilibria, Phase Diagrams and Phase Transformations: Their Thermodynamic Basis*, Cambridge University Press, 2007.
27 D. A. Porter, K. E. Easterling and K. E. Easterling, *Phase Transformations in Metals and Alloys (Revised Reprint)*, CRC Press, 2009.
28 N. Meethong, H. Y. S. Huang, W. C. Carter and Y. M. Chiang, *Electrochem. Solid-State Lett.*, 2007, **10**, 134–138.
29 P. Gibot, M. Casas-Cabanas, L. Laffont, S. Levasseur, P. Carlach, S. Hamelet, J. M. Tarascon and C. Masquelier, *Nat. Mater.*, 2008, **7**(9), 741–747.
30 G. Kobayashi, S. I. Nishimura, M. S. Park, R. Kanno, M. Yashima, T. Ida and A. Yamada, *Adv. Funct. Mater.*, 2009, **19**, 395–403.
31 H. Liu, F. C. Strobridge, O. J. Borkiewicz, K. M. Wiaderek, K. W. Chapman, P. J. Chupas and C. P. Grey, *Science*, 2014, **344**, 1252817.
32 G. K. Singh, G. Ceder and M. Z. Bazant, *Electrochim. Acta*, 2008, **53**, 7599–7613.
33 G. Chen, X. Song and T. J. Richardson, *Electrochem. Solid-State Lett.*, 2006, **9**, A295.
34 Y. Zhu, J. Wei Wang, Y. Liu, X. Liu, A. Kushima, Y. Liu, Y. Xu, S. X. Mao, J. Li, C. Wang, J. Yu Huang, Y. Zhu, Y. Liu, Y. Xu, C. Wang, J. W. Wang, S. X. Mao, X. Liu, J. Y. Huang, A. Kushima and J. Li, *Adv. Mater.*, 2013, **25**, 5461–5466.
35 J. Niu, A. Kushima, X. Qian, L. Qi, K. Xiang, Y.-M. Chiang and J. Li, *Nano Lett.*, 2014, **14**, 4005–4010.
36 Y.-S. Yu, M. Farmand, C. Kim, Y. Liu, C. P. Grey, F. C. Strobridge, T. Tyliszczak, R. Celestre, P. Denes, J. Joseph, H. Krishnan, F. R. N. C. Maia, A. L. D. Kilcoyne, S. Marchesini, T. P. C. Leite, T. Warwick, H. Padmore, J. Cabana and D. A. Shapiro, *Nat. Commun.*, 2018, **9**, 921.
37 B. M. May, Y.-S. Yu, M. V. Holt, F. C. Strobridge, U. Boesenberg, C. P. Grey and J. Cabana, *Nano Lett.*, 2017, **17**, 7364–7371.
38 E. R. Logan, A. Eldesoky, Y. Liu, M. Lei, X. Yang, H. Hebecker, A. Luscombe, M. B. Johnson and J. R. Dahn, *J. Electrochem. Soc.*, 2022, **169**, 050524.
39 M. Haataja and F. Léonard, *Phys. Rev. B: Condens. Matter Mater. Phys.*, 2004, **69**, 081201.
40 *Solids Far from Equilibrium*, ed. G. Claude, Cambridge University Press, USA, 1992.
41 N. Moelans, B. Blanpain and P. Wollants, *CALPHAD: Comput. Coupling Phase Diagrams Thermochem.*, 2008, **32**, 268–294.
42 M. S. Islam, D. J. Driscoll, C. A. J. Fisher and P. R. Slater, *Chem. Mater.*, 2005, **17**, 5085–5092.
43 L. Hong, L. Li, Y.-K. Chen-Wiegart, J. Wang, K. Xiang, L. Gan, W. Li, F. Meng, F. Wang, J. Wang, Y.-M. Chiang, S. Jin and M. Tang, *Nat. Commun.*, 2017, **8**, 1194.